HHS Public Access

Author manuscript

Neuroimage. Author manuscript; available in PMC 2022 February 15.

Published in final edited form as:

Neuroimage. 2022 February 15; 247: 118793. doi:10.1016/j.neuroimage.2021.118793.

Focal fMRI signal enhancement with implantable inductively coupled detectors

Yi Chen[a,b,#], **Qi Wang**[a,c,#], **Sangcheon Choi**[a,c], **Hang Zeng**[a,c], **Kengo Takahashi**[a,c], **Chunqi Qian**[d,*], **Xin Yu**[e,*]

[a]Max Planck Institute for Biological Cybernetics, 72076 Tuebingen, Germany

[b]Max Planck Institute for the Science of Light, 91058, Erlangen, Germany

[c]Graduate Training Centre of Neuroscience, University of Tuebingen, 72076 Tuebingen, Germany

[d]Department of Radiology, Michigan State University, East Lansing, MI 48824, USA

[e]Athinoula A. Martinos Center for Biomedical Imaging, Massachusetts General Hospital and Harvard Medical School, Charlestown, MA 02129, USA

Abstract

Despite extensive efforts to increase the signal-to-noise ratio (SNR) of fMRI images for brain-wide mapping, technical advances of focal brain signal enhancement are lacking, in particular, for animal brain imaging. Emerging studies have combined fMRI with fiber optic-based optogenetics to decipher circuit-specific neuromodulation from *meso* to macroscales. High-resolution fMRI is needed to integrate hemodynamic responses into cross-scale functional dynamics, but the SNR remains a limiting factor given the complex implantation setup of animal brains. Here, we developed a multimodal fMRI imaging platform with an implanted inductive coil detector. This detector boosts the tSNR of MRI images, showing a 2–3-fold sensitivity gain over conventional coil configuration. In contrast to the cryoprobe or array coils with limited spaces for implanted brain interface, this setup offers a unique advantage to study brain circuit connectivity with optogenetic stimulation and can be further extended to other multimodal fMRI mapping schemes.

[*]Corresponding authors: qianchu1@msu.edu (C. Qian), xyu9@mgh.harvard.edu (X. Yu).
[#]These authors contributed equally to this work.

Credit author statement
Yi Chen: Investigation, Formal analysis, Writing-Original Draft, Writing - Review & Editing
Qi Wang: Investigation, Formal analysis, Writing-Original Draft.
Sangcheon Choi: Formal analysis
Hang Zeng: Validation
Kengo Takahashi: Validation
Chunqi Qian: Methodology, Conceptualization, Supervision, Resources, Writing-Review&Editing, Project administration.
Xin Yu: Methodology, Conceptualization, Supervision, Resources, Writing-Review&Editing, Project administration, Funding acquisition.

Declaration of Competing Interest
The authors declare no competing interests.

Code availability
The related image processing codes are available from the corresponding authors upon request.

Supplementary materials
Supplementary material associated with this article can be found, in the online version, at doi:10.1016/j.neuroimage.2021.118793.

Keywords

Optogenetics; Layer-specificity; Inductively Coupled Detectors; SNR enhancement; fMRI

1. Introduction

The combination of fMRI with optogenetics presents a promising tool for mechanistic studies of neuromodulation with cellular and circuit specificity from meso- to macro-scales (Lee et al., 2010; Liang et al., 2015; Ferenczi et al., 2016; Ryali et al., 2016; Yu et al., 2016; Albers et al., 2018a; Iordanova et al., 2018; Chen et al., 2019; Jung et al., 2021). However, given indirect measurements of neuronal activity with fMRI (Ogawa et al., 1992; Logothetis et al., 2001; Logothetis 2008), it remains ambiguous to represent the circuit-specific brain activation based on global hemodynamic patterns, *e.g.,* the blood-oxygen-level-dependent (BOLD) functional maps (Logothetis 2010). Besides brain-wide functional imaging, high-resolution fMRI of focal brain regions has emerged to map laminar-specific BOLD signal across cortical layers (Silva and Koretsky 2002; Goense and Logothetis 2006; Chen et al., 2013; Yu et al., 2014; Huber et al., 2017; Albers et al., 2018a; Kashyap et al., 2018a; Finn et al., 2019; Sharoh et al., 2019; Yu et al., 2019; Han et al., 2021). This unique mapping scheme improves the spatial specificity of fMRI when mapping neuronal projection patterns in different cortices and the olfactory bulb (Yu et al., 2014; Poplawsky et al., 2015; Huber et al., 2017; Nunes et al., 2019; Poplawsky et al., 2019; Sharoh et al., 2019; Han et al., 2021). Recently, there has been an increasing trend to apply laminar fMRI for human brain mapping with either top-down or bottom-up tasks (Huber et al., 2017; Kashyap et al., 2018; Finn et al., 2019; Sharoh et al., 2019; Yu et al., 2019). In contrast to human laminar fMRI, animal laminar fMRI combined with optogenetics has demonstrated a unique platform to elucidate the circuit-specific regulatory mechanism underlying varied BOLD responses across different layers (Albers et al., 2018a; Jung et al., 2021).

An ongoing challenge of laminar fMRI is the limited signal-to-noise ratio (SNR) when sampling the layer-specific BOLD signal with high resolution. Using high field (>11.7 Tesla) MR scanners, researchers have developed a line-scanning fMRI method to extract BOLD signals with sufficient SNR across cortical layers (Yu et al., 2014; Sangcheon Choi 2021). Albers et al. have applied the line-scanning fMRI to detect the layer-specific BOLD responses driven by optogenetic stimulation in rodent brains (Albers et al., 2018a). However, given the implantation of optical fiber, it remains challenging to apply the advanced cryoprobe (Darrasse and Ginefri 2003; Baltes et al., 2009; Takata et al., 2015; Schlegel et al., 2018) or multi-array radio frequency (RF) coils (Roemer et al., 1990; Gareis et al., 2007) for focal signal enhancement. Although several studies have accommodated cryoprobes with optical fiber implantation, the fiber has to be inserted horizontally along the posterior-anterior axis of the rat brain (Takata et al., 2015; Schlegel et al., 2018), creating much tissue damage. Also, even with the surface coil designed to accommodate optical fiber implantation (Yu et al., 2016; Chen et al., 2019a; Pais-Roldan et al., 2020), the adhesive surgical material used to fix the fiber at the skull creates a considerable distance between the surface coil and brain regions, further restricting the acquisition of laminar fMRI signal with sufficient SNR.

To reduce hardware complexity and to boost sensitivity, several groups have applied inductively coupled detectors (ICD) to relay locally detected MR signals with an external surface RF coil wirelessly (Schnall et al., 1986; Wirth et al., 1993; Volland et al., 2010; Ginefri et al., 2012; Mett et al., 2016). Specifically, the ICD-mediated mapping scheme has been used for animal MRI. For example, Volland et al. developed an inductively coupled MR coil system for imaging and spectroscopic analysis of an implantable bioartificial construct in mice peritoneal cavity at 11.1 T (Volland et al., 2010). And, Ginefri et al. fabricated an inductively-coupled coil fitted to the interhemispheric cleft and improved anatomical image SNR of rat brains at 7 T (Ginefri et al., 2012). All these studies demonstrated sensitivity enhancement in very close proximity to the targeted ROI with ICD. Despite the promising prospects of animal MR studies, ICDs have not been well utilized in the multi-modal platform to solve the abovementioned challenging issues.

Hence, as a proof-of-concept demonstration, to improve MR detection sensitivity for cross-scale brain mapping, we presented an optimized multimodal fMRI platform with ICDs. Whole-brain echo-planar imaging (EPI) and line-scanning fMRI were performed in anesthetized rat brains to verify the SNR improvement with ICDs. Moreover, as an *in vivo* benchmark application of ICD in contrast to conventional surface coils, we have embedded the ICD with optical fiber implantation to show a near 3-fold enhancement of SNR in optogenetically-driven laminar BOLD fMRI experiments.

2. Material and methods

2.1. Flexible implanted inductive coil design and fabrication

Based on the wireless inductive coupling theorem, we used the inductive coil design with a smaller-dimension circuit to maintain detection sensitivity (Fig. 1a). The inductive coil was tuned to 599.58 MHz by the formula: $f = \frac{1}{2\pi\sqrt{LC}}$, matching the resonance frequency delivered by a transceiver coil in a 14.1 T scanner. Hence, the value of inductance (L) determines the dimension of the conductor, and the tuning capacitance was adjusted to maintain constant resonance frequency. The fabrication process is described as below: first, we print the conductor with copper material on a printed circuit board (PCB, by Electronics Workshop of Max Planck Institute for Biological Cybernetics, Tübingen, Germany), in a circle with a dimension of 1 mm strip width, 6 mm outer diameter; then, we mount the capacitor, which is an unbiased diode (BBY5302VH6327XTSA1, Infineon Technologies, Germany); solder and assemble the designed circuit (Fig. 1b). For the expression of the on-bench performance of inductive coil, its frequency response profile was color mapped under different distance separations from 0 mm to 25 mm with a step size of 1 mm, using *imagesc* function of MATLAB (Fig. 1c).

2.2. Animals

The study was performed in accordance with the German Animal Welfare Act (TierSchG) and Animal Welfare Laboratory Animal Ordinance (TierSchVersV), in full compliance with the guidelines of the EU Directive on the protection of animals used for scientific purposes (2010/63/EU). The study was reviewed by the ethics commission (§15 TierSchG) and approved by the state authority (Regierungspräsidium, Tübingen, Baden-Württemberg,

Germany). A 12–12 h on/off lighting cycle was maintained to assure undisturbed circadian rhythm. Food and water were available *ad libitum*. This study used a total of 6 male Sprague–Dawley rats acquired from Charles River.

2.3. Viral injection and immunohistochemistry

As reported previously (Yu et al., 2016; Chen et al., 2019a; Chen et al., 2019b), AAV5.CaMKII.hChR2 (H134R)-mCherry (100 μL at titer ≥ 1×10^{13} vg/mL) from Addgene was injected in 4-week-old rats intracerebrally in the right somatosensory forepaw region. Rats were anesthetized with 1.5–2% isoflurane via a nose cone and placed on a stereotaxic frame. An incision was made on the scalp to expose the skull. Craniotomies were performed with a pneumatic drill to introduce minimal damage to cortical tissue. A volume of 0.6–0.9 μL was injected using a 10-μL syringe and 33-gage needle to the stereotaxic coordinates: 0 mm posterior to Bregma, 3.8–4.0 mm lateral to the midline, 0.8–1.4 mm below the cortical surface. After injection, the needle was left in place for approximately 5 min before being slowly withdrawn. The craniotomies were sealed with bone wax, and the skin around the wound was sutured. Rats were injected with antibiotics and painkillers (Ketoprofen fluids) subcutaneously for three consecutive days to prevent bacterial infections and relieve postoperative pain.

Immunostaining was performed to verify the ChR2 expression and implanted fiber localization in the brain. Perfused rat brains were fixed overnight in 4% paraformaldehyde and then equilibrated in 15% and 30% sucrose with 0.1 M PBS at 4 °C. We used cryotome (CM3050S, Leica, Germany) to Section 30 μm brain slice. Free-floating brain slices were washed in PBS, mounted on microscope slides, and incubated with DAPI (VectaShield, Vector Laboratories, USA) for 30 mins at room temperature. We acquired wide-field fluorescent images (Zeiss, Germany) to examine ChR2 expression in the FP-S1. Digital images were minimally processed using ImageJ to enhance brightness and contrast for visualization purposes.

2.4. Animal preparation, inductive coil/fiber optic implantation for fMRI

Animals were anesthetized with 5% isoflurane in a chamber and maintained with 2% isoflurane during surgeries. Throughout the experiment, the anesthetized rat was intubated using a tracheal tube and ventilated by a mechanical ventilator (SAR-830, CWE, USA). Femoral arterial and venous were catheterized using polyethylene tubes for blood sampling, drug administration, and constant blood pressure measurements. After the surgery, a bolus of the alpha-chloralose (80 mg/kg) was injected intravenously through the femoral vein. A mixture of alpha-chloralose (26.5 mg/kg/h) and pancuronium (2 mg/kg/h) was constantly infused to keep the animal anesthetized and reduce respiration-induced motion artifacts during MR scanning.

Before transferring the animal into the MRI scanner, we placed it on a stereotaxic frame. For electrical stimulation as shown in Fig. 2, the 6 mm single loop inductive coil was directly positioned on the skull above the right FP-S1 region, which was fixed on the skull with adhesive gel (Loctite 454, Henkel, Germany) beneath the 22 mm surface coil (Fig. 2a, b). The distance between the surface coil and the ICDs was approximately 2.5 mm (the PCB

thickness of the surface coil plus that of the ICD). For the optogenetic experiment in Fig. 3, we drilled a ~1.5 mm diameter burr hole on the skull and carefully removed the dura. An optical fiber with a 200-μm core diameter (FT200EMT, Thorlabs, Germany) was inserted into the FP-S1 through the hole of a 6-mm inductive coil, at coordinates of 0 mm posterior to Bregma, 4 mm lateral to the midline and 1.2–1.4 mm below the cortical surface. We used an adhesive gel (Loctite 454, Henkel, Germany) to secure the fiber to the skull with the inductive coil detector. Then we closed the scalp by glue with the head post setup. At the same time, we placed the other 6-mm inductive coil on the projected FP-S1 in the left hemisphere. Black tapes were used to cover the rat eyes to prevent stimulation of the visual system during optogenetic stimulation.

2.5. MRI acquisition

All images were acquired with a 14.1 T/26 cm horizontal bore magnet interfaced to an AVANCE III console and equipped with a 12 cm gradient set capable of providing 100 G/cm over a time of 150 μs. We used a transceiver single-loop surface coil and inductive coils as described above to acquire MRI images.

The FLASH images in Fig. 1d for phantoms were acquired with the following parameters: TR/TE 100/5 ms, excitation pulse angle 30°, slice thickness 0.2 mm, FOV 4 cm × 4 cm, and matrix 256 × 256. Functional images in Fig. 2d, e were acquired with a 3D gradient-echo EPI sequence with the following parameters: TE, 11.5 ms, TR, 1.5 s, FOV 1.92 × 1.92 × 1.92 cm, matrix size 48 × 48 × 48, spatial resolution 0.4 × 0.4 × 0.4 mm. We applied a 2D RARE sequence to acquire 48 coronal slices with the same geometry as fMRI images. The FLASH-based bilateral line-scanning fMRI was performed with two saturation slices to dampen the MR signal outside the regions of interest (Fig. 2e) with the following parameters: TR/TE 100/5 ms, excitation pulse angle 30°, slice thickness 1 mm, FOV 6.4 × 3.2 mm and matrix 64 × 32. The phase-encoding gradient was turned off. Given the small size of the transceiver, the RF power calibration (*i.e.*, calculating an appropriate flip angle to be assigned for a given case) was based on the slice covering brain regions. Here, we set the slice center at the middle cortical layer when calibrating the power of the RF pulse. Thus, the excitation pulse angle is typically optimized at the middle layer of the cortex.

We performed electrical stimulation on the left forepaw (3 Hz, 4 s, 300 μs width, 2 mA) and optogenetic stimulation on the right FP-S1 (2 Hz, 6 s, light pulse width 10 ms, 30 mW) to activate the neurons expressing ChR2 (Fig. 3a). The block design paradigm included 1 s pre-stimulation, 4 s stimulation on (6 s for optogenetic stimulation), and 15 s intervals (13 s for optogenetic stimulation), *i.e.*, 20 s for each epoch and 32 epochs for a full trial (10 m 40 s). We tested the light pulse (2 Hz) optogenetic stimulation with the power level from 0.6 to 40 mW (Chen et al., 2020). 30 mW light pulse stimulation was used to induce positive BOLD responses in the contralateral cortical regions. Given the short stimulation duration, we did not observe the heat-induced negative BOLD signal with the whole-brain 3D-EPI fMRI experiment, as shown in Fig. S6.

2.6. Data analysis

All signal processing and analyses were implemented in MATLAB software (Mathworks, Natick, MA) and Functional NeuroImages software (AFNI, NIH, USA). For evoked fMRI analysis of Fig. 2d, e, Fig. S2, and S6, to generate BOLD functional maps, we applied pre-processing steps including motion correction, image registration, time course normalization and averaged fMRI datasets from multiple trials for each animal. The regression analysis of hemodynamic response function (HRF) was based on the BLOCK function of the linear program 3dDeconvolve in AFNI. BLOCK (d, 1) computes a convolution of a square wave of duration d and makes a peak amplitude of block response = 1.

$$HRF(t) = int(g(t-s), s = 0..\min(t, d))$$

where $g(t) = t^q e^{-t}/[q^q e^{-q}]$, where $q = 4$, d = duation of a square wave. Each beta weight represents the peak height of the corresponding BLOCK function.

For layer-specific fMRI analysis, the boundaries of cortices were defined based on the reference position of both cortical surface and corpus callosum. The cortical surface was determined at half the maximum signal intensity of the 1d profile along with the cortical depth (Yu et al., 2014). As a function of time, fMRI percentage dynamics were calculated based on the following equation: $SI_{percetage} = (SI_i - SI_{baseline})/SI_{baseline}$, where SI_i denotes signal intensity at the i^{th} time point, i = 0:0.1:20 s for each epoch, and $SI_{baseline}$ indicates the mean value of signal intensity at pre-stimulation duration (1 s). Such time series of activation were presented and color-coded after averaging voxel-wise dynamics of the entire cortex (Fig. 2f top right, and Fig. 3b top) through whole scan duration (Fig. 2f top left, Fig. 3a top left and right). Likewise, laminar-specific activation features were averaged within each layer, respectively (Fig. 3c). For epoch-wise spatiotemporal activations, time series were averaged for each voxel and were color-mapped (*imagesc* function in MATLAB), where the signal intensity was expressed in percentages (Fig. 2f bottom right and Fig. 3b bottom). Due to the contribution of large draining veins on the cortical surface, higher values of BOLD changes exist in voxels close to the cortical surface.

For resting-state fluctuation of hemodynamics, z-normalized time series (*zscore* function in MATLAB) of a single trial were demeaned to present overall cortical fluctuation (Fig. 2g top). As to the spatiotemporal map with whole scan duration, we applied the bandpass filter of 0.01–0.1 Hz through zero-phase digital filtering (*filtfilt* function in MATLAB) and standardized intensity values between 0 and 1 per voxel of the cortex (Fig. 2f lower left, Fig. 3a lower left and right).

Fig. 2c, Fig. 1d, and Fig. S1b illustrate the comparison of SNR by a bar plot containing the enhanced region and the normal one encircled by identical geometries. SNR was calculated by:

$$SNR_j = \frac{\overline{SI_j}}{\sigma_{background}}$$

where $\overline{SI_j}$ stands for the mean of signal intensity in the regions of interest labeled by j, indicating enhanced or uncovered region, and $\sigma_{background}$ stands for the standard deviation of signal intensity in a sample of background. The console of the BRUKER system adjusted the RF pulse attenuation automatically. Black dots in the figures mentioned above indicate SNR values of individual animals, and error bars indicate standard deviation (s.d.) for all the animals.

Fig. 2g (right) and Fig. 3d compared temporal Signal-to-Noise-Ratio (tSNR) between before and after inductive coupling enhancement, tSNR was calculated as:

$$tSNR_k = \frac{\overline{SI_k}}{\sigma_k}$$

Where $\overline{SI_k}$ stands for the averaged amplitude of signal time series during the scan of the corresponding animal, and σ_k for the standard deviation of the corresponding time series, both variants were made after averaging the signal intensity over the entire cortical depth.

A paired-sample t-test for both sets of data (*ttest2* function in MATLAB) calculates the statistical significance, where the shading region covers a range of paired voxels with distinct levels of statistical significance (Fig. 2g right and Fig. 3d), *i.e.*, $^{**}P < 0.01$. Likewise, bar markers of significance level were calculated after averaging tSNR value of animals in each group, with error bars expressing s.d. of individual trials.

3. Results

3.1. *Design, characterization, and* ex vivo *evaluation of the inductive coil detector (ICD)*

We fabricated a 6-mm single-ring ICD whose performance with sample loading conditions was evaluated on-bench and inside a 14.1 T scanner. Fig. 1a demonstrated the proposed single-ring ICD and a conceptual diagram for bench measurements. The proposed setup consists of a single-ring ICD, and a conventional transceiver surface coil, while NMR signals from the insulated ICD can be transmitted to the external coil through mutual inductive coupling (Fig. 1b). The single-loop ICD was placed on top of a 1% agarose gel phantom while the conventional surface coil placed above the phantom with a specific distance separation would provide RF excitation pulse and receive amplified signals from ICD (Fig. 1a–b). No modifications to the scanner interface were required. As shown in Fig. 1c, the strong coupling effect between the ICD and surface coil could be maintained for a distance as large as 12 mm. A representative image for the gel phantom was shown in Fig. 1d (left), and the relative SNR from the focal region below the ICD is shown in Fig. 1d (right). The excitation pulse transiently detuned the ICD during RF excitation, so the sample was excited directly by the external surface coil. As we gradually moved the external RF coil away from the sample surface (Fig. 1d), more power was required on the surface coil to excite nuclei spins, leading to smaller “RF pulse attenuation”. During MR signal reception, because the ICD always detected MR signals before being inductively coupled to the external RF coil, superior local sensitivity can be maintained within a specific distance separation, as long as inductive coupling remains larger than circuit loss (Fig. 1d right). *In*

vitro test results detected the effective distance (<12 mm) between the ICD and the surface coil for inductive coupling.

3.2. In vivo *evaluation of ICD with layer-specific BOLD fMRI mapping in rat brains*

Next, ICD was evaluated *in vivo* to measure enhanced fMRI signal in the right forepaw somatosensory cortex (FP-S1) with unilateral electrical forepaw stimulation and during resting state in anesthetized rats (Fig. 2). A 6-mm single loop inductive coil was embedded beneath the 22 mm surface coil at the right FP-S1 (Fig. 2a). By relaying locally detected MR signals to the external surface coil, the focal intensity enhancement by this ICD with a 6 mm diameter was detected throughout the 2 mm cortex from anatomical FLASH MR images (Fig. 2b). The focal signal intensity in ROI 1 below the ICD in the right FP-S1 was significantly higher than that of ROI 2 in the left hemisphere without ICD (Fig. 2b, c). Furthermore, the signal intensity was comparable to that acquired using a conventional 10-mm surface coil attached on the rat brain, indicating that ICD can well compensate the B1 sensitivity-related signal loss due to the extra space introduced between the cortex and the surface coil (Fig. S1). As shown in Fig. 2d (Fig. S2 for another two rats), the anatomical image with superimposed BOLD functional maps demonstrated that the ICD-enhanced region was well overlapped with the most activated FP-S1. Besides the EPI-based BOLD, we acquired laminar-specific BOLD responses with 100 ms temporal resolution and 100-μm spatial resolution using line-scanning fMRI (Fig. 2e). The time courses and line profile-based 2D fMRI maps across cortical layers were presented in stimulation (Fig. 2f) and resting-state conditions (Fig. 2g). The tSNR for resting-state brain fluctuation in the cortex illustrated that the ICD was up to 2-fold more sensitive than the surface coil only condition when implantation introduced extra space to reduce the B1 sensitivity of the surface coils (Fig. S3 and Fig. 2g, paired-sample t-test, $^{***}P < 0.001$), with negligible contamination from motion and respiration noise and vascular pulsation (Fig. S4 and Fig. S5).

3.3. Evaluation of ICD at multimodal fMRI platform with optogenetic-driven layer-specific BOLD mapping

Combining optical fiber-based optogenetic stimulation and bilateral line-scanning fMRI (Sangcheon Choi 2021) verified the high sensitivity of ICD. We embedded two ICDs to cover the FP-S1 of both hemispheres with optical fiber implanted to target the right FP-S1 expressing channelrhodopsin-2 (ChR2) (Fig. 3a, middle). Fig. S6a showed the images acquired with two inductive coils. Upon optogenetic stimulation, robust BOLD responses were detected in the right FP-S1 region (Fig. 3a, right) and evoked BOLD signal in the left FP-S1 region (Fig. 3a, left). The whole-brain BOLD fMRI mapping was shown in Fig. S6b. Moreover, the averaged line profile-based 2D fMRI maps (Fig. 3b) and time courses (Fig. 3c) were displayed to represent the layer-specific hemodynamic responses. Interestingly, the evoked BOLD signals in the left FP-S1 contralateral to the optogenetic stimulation showed salient post-stimulus undershoots in L2/3 and L5, indicating a transcallosal projection-mediated interhemispheric inhibition (Karayannis et al., 2007; Palmer et al., 2012; Chen et al., 2020). Also, the laminar-specific tSNR with ICD showed up to a 3-fold SNR increase over the bilateral line-scanning fMRI signals detected only with the surface coil (Fig. 3d, blue and red line, respectively, paired-sample t-test, $^{***}P < 0.001$). This result demonstrated

the unique advantage of boosting the SNR with ICD-based optogenetic laminar-fMRI. Moreover, the ICD-based mapping scheme with high SNR could enable single-vessel fMRI mapping (Fig. S7) (Yu et al., 2016; He et al., 2018; Chen et al., 2019a), which will be further combined with optical fiber-mediated optogenetics or genetically encoded biosensor recordings. These results demonstrated the broader application of the ICD-based mapping scheme to acquire sufficient SNR in high-resolution fMRI images.

4. Discussion

This study presents a multimodal platform by combining optogenetics and line-scanning fMRI in animals with implanted ICD (Inductively Coupled Detector) to increase the SNR of fMRI images. Conventional surface coils have been used for focal signal enhancement when attaching miniaturized coils to cortical regions (Ackerman et al., 1980; Chen et al., 2019a). In particular, surface coils can accommodate the optogenetic setup with fiber bundles passing through the open area of the coil. It should also be noted that implanting optical fiber to the target brain region will introduce a considerable distance separation between the RF coil and cortical regions, leading to significantly reduced B1 sensitivity for focal brain signal detection. We developed the ICD to overcome this limitation through implantation close to the cortical region, which can be wirelessly coupled to an external surface coil over a distance (Wirth et al., 1993; Volland et al., 2010; Ginefri et al., 2012; Mett et al., 2016).

The ICD design shows several advantages in comparison to cryoprobe design for multi-modal functional mapping with implanted optical fibers in animals. Given the insulated ceramic holder design required for cryoprobe to maintain its superconducting feature inside cryogen (Styles et al.,1989), it is impossible to penetrate an optical fiber through the cryoprobe. In several studies, the optical fiber has been inserted along the posterior-to-anterior axis of the brain to target cortex or subcortical regions, allowing the application of cryoprobe for multi-modal fMRI imaging (Takata et al., 2015; Schlegel et al., 2018). Although the SNR can be significantly increased with cryoprobe, the horizontal orientation required for optical fiber insertion makes it less practical for precise targeting of brain nuclei, producing relatively large collateral damage through the cerebellum. In addition, the optical fiber has to be secured on the skull with minimal space for fixation material to ensure the sufficient B1 sensitivity of the cryoprobe. In contrast, our ICD design can be directly attached to the skull during optical fiber implantation and transmit the RF signal through the pickup coil. This wireless ICD design can be extended to target different brain regions using multiple ICD components, producing 2–3-fold sensitivity gain over conventional surface coils (Fig. 2g and Fig. 3d). Although the ICD-based SNR gain is comparable to cryoprobe, it simplifies experimental setup and free more open space inside the scanner for other complementary imaging modalities, *e.g.*, fluorescent calcium recording (Schulz et al., 2012; Liang et al., 2017; Albers et al., 2018b; Wang et al., 2018; Lake et al., 2020), pupillometry (Pais-Roldan et al., 2020) and optogenetics in awake rodents (Desai et al., 2011; Liang et al., 2015; Ferenczi et al., 2016; Gao et al., 2017).

To validate the unique advantage of ICD-based focal signal enhancement, we implemented ICD for the bilateral line-scanning fMRI with optogenetics. The line-scanning fMRI method

has been developed to extract the layer-specific BOLD signal from focal brain regions with a high spatial resolution, facilitating the emerging laminar fMRI studies from animal to human brains (Silva and Koretsky 2002; Goense and Logothetis 2006; Chen et al., 2013; Yu et al., 2014; Huber et al., 2017; Albers et al., 2018a; Kashyap et al., 2018a; Finn et al., 2019; Sharoh et al., 2019; Yu et al., 2019; Raimondo et al., 2021). The high resolution laminar-specific mapping scheme provides a unique strategy to map the circuit-specific neuronal connectivity through a large spatial scale. To date, the spatiotemporal dynamic patterns of evoked fMRI signals through transcallosal projections have not been thoroughly investigated. Here, two ICDs were used to map the interhemispheric laminar fMRI signals with sufficient SNR following optogenetic stimulation in the FP-S1 of one hemisphere. The salient post-stimulus undershoots detected in Layer 2/3 and 5 (Fig. 3) present the unique coupling feature of hemodynamic responses related to the interhemispheric excitatory/inhibitory balance (Chen et al., 2020). Brain slice electrophysiological recording has revealed that callosal circuit-mediated glutamatergic excitatory postsynaptic potentials are followed by elongated GABA-mediated inhibitory postsynaptic potentials (Kawaguchi 1992; Kumar and Huguenard 2001; Karayannis et al., 2007; Palmer et al., 2012). The optogenetically driven callosal activity has been used to disentangle circuit-specific interhemispheric inhibitory effects, *e.g.,* in the auditory cortex (Rock and Apicella 2015), prefrontal cortex (Lee et al., 2014), and hindlimb somatosensory cortex (Palmer et al., 2012). Interestingly, Iordanova et al. revealed transcallosal-mediated hemodynamic responses into three major categories: negative, biphasic, and no-response, with hemoglobin-based optical intrinsic signal imaging following optogenetic stimulation (Iordanova et al., 2018). Also, Hoffmeyer and colleagues reported the nonlinear neurovascular coupling in rat sensory cortex upon direct electrical stimulation of transcallosal pathways (Hoffmeyer et al., 2007). It will be interesting to further elucidate the controversial positive/negative BOLD signals contributed from excitatory/inhibitory neuronal activity using optogenetics (Iordanova et al., 2018; Vazquez et al., 2018; Moon et al., 2021), especially for the diverse neurovascular coupling features along the interhemispheric circuits with layer-specificity. Our work provides the possibility to deepen the mechanistic understanding of laminar-connectivity either through corticocortical or subcortical connections with ICD-based multi-slice line scanning fMRI (Yu et al., 2014; Albers et al., 2018a; Jung et al., 2021). It should also be noted that although the ICD increased the tSNR of laminar fMRI signals, the BOLD responses driven by callosal projections still have low contrast-to-noise ratio as shown in Fig 3b. To compare the bilateral BOLD temporal dynamics, a massive averaging scheme remains necessary in future studies.

Several limitations about the usage of ICD in the multi-modal fMRI platform should be considered when interpreting the results of this work and for future optimization of the ICD for high field animal fMRI. First, although the ICD has a 2–3-fold sensitivity gain over the external surface coil, it is coupling with the external surface coil passively, thus limiting its effective distance separation from the external surface coil. Also, the signal gain reported in our study is based on the comparison with the large surface coil (~20 mm). We did not compare the ICD with the small diameter surface RF coil (*e.g.,* 6–10 mm) because the B1 sensitivity is attenuated by the increased distance separation between the detector and the cortical regions of interests. Significant signal loss will occur if the surface coil

is positioned above the implanted rat brain with large distance separations. On the other hand, it is well established that wirelessly amplified NMR detector (WAND) can efficiently amplify MRI signals, leading to an additional >3-fold sensitivity gain over passive coupling (Qian et al., 2013; Qian et al., 2020), especially for larger distance separations. Therefore, it will be helpful to utilize the WAND to improve the effective operation range of implantable detectors. Secondly, even for passive coupling, there is still room for further improvement. For example, the angle between the external surface coil and the inductive coil should be as parallel as possible, ensuring a higher coupling coefficient between the two coils. Typically, the parallel arrangement can be implemented readily in phantoms. However, for *in vivo* experiments, the inductive coil is implanted on top of the curved skull, making parallel arrangement harder. This procedure explains the 6–7 fold sensitivity gain for *in vitro* experiments (Fig. 1d) in comparison to the only 2–3 fold enhancement for *in vivo* experiments (Fig. 2g and Fig. 3d). Moreover, through increasing the averaged tSNR, the SEM (Standard Error of the Mean) with ICD has larger variance across the cortical layers than the SEM without ICD (Fig. 2g and Fig. 3d), because of the different coupling coefficient for each *in vivo* experiment. Also, the tSNR across different cortical layers did not show expected monotonic decay with increased distance from the coil (Fig. 2g, Fig. 3d, and Fig. S3) because of the transceiver-based slice excitation scheme (See Method section). Thirdly, although we only discussed focal signal enhancement with ICD, it is also possible to develop the wireless, implantable array of ICDs to enhance the detection sensitivity of the entire brain (Bulumulla et al., 2015). In contrast to the conventional RF coil array requiring multiple detection channels, multiple ICDs can be combined for multiple channel RF sensing of MR signals through different bandwidths using one channel. Different from the two ICD component position as shown in Fig. 3 and Fig. S6, adjacent ICDs can be partially overlapped to decouple their signal interference. Moreover, resonant decoupler can be utilized to remove signal interference from non-adjacent ICDs for the ICD-based wireless array design (Alipour et al., 2020).

5. Conclusions

In summary, we have implemented ICDs in the multimodal imaging platform to yield high-resolution structural and functional images of the rat brain with high SNR. The ICD-based mapping scheme facilitates optogenetic-driven brain connectivity studies with a simplified environmental setup.

Supplementary Material

Refer to Web version on PubMed Central for supplementary material.

Acknowledgements

This research was supported by NIH Brain Initiative funding (RF1NS113278, R01 MH111438, R01NS122904), NSF grant 2123971, and the S10 instrument grant (S10 MH124733-01) to Martinos Center, German Research Foundation (DFG) Yu215/3-1, Yu315/2-1, BMBF 01GQ1702, and the internal funding from Max Planck Society. This project has received funding from the European Union Framework Programme for Research and Innovation Horizon 2020 (2014–2020) under the Marie Skłodowska-Curie Grant Agreement No.896245. We thank Dr. MH. Frosz, Mr. J Walzog, Dr. R. Pohmann, Dr. J. Engelmann, Dr. N. Avdievitch and Ms. H. Schulz for technical support, Dr. P. Douay and Ms. R. König for animal support, the AFNI team for the software support.

Data availability

The data that support the findings of this study are available from the corresponding authors upon request.

Glossary

fMRI	functional Magnetic Resonance Imaging
BOLD	Blood oxygen level dependent
SNR	signal-to-noise ratio
ICD	Inductively Coupled Detectors
EPI	echo-planar imaging

References

Ackerman JJH, Grove TH, Wong GG, Gadian DG, Radda GK, 1980. Mapping of metabolites in whole animals by P-31 NMR using surface coils. Nature 283 (5743), 167–170. [PubMed: 7350541]

Albers F, Schmid F, Wachsmuth L, Faber C, 2018a. Line scanning fMRI reveals earlier onset of optogenetically evoked BOLD response in rat somatosensory cortex as compared to sensory stimulation. Neuroimage 164, 144–154. [PubMed: 28012967]

Albers F, Wachsmuth L, van Alst TM, Faber C, 2018b. Multimodal functional neuroimaging by simultaneous BOLD fMRI and fiber-optic calcium recordings and optogenetic control. Mol Imaging Biol 20 (2), 171–182. [PubMed: 29027094]

Alipour A, S. A.C., Delman B, Adriany G, Balchandani P (2020). "Improvement of brain MRI at 7T using an inductively coupled RF resonator array." https://arxiv.org/abs/2006.02500.

Baltes C, Radzwill N, Bosshard S, Marek D, Rudin M, 2009. Micro MRI of the mouse brain using a novel 400 MHz cryogenic quadrature RF probe. NMR Biomed. 22 (8), 834–842. [PubMed: 19536757]

Bulumulla SB, Fiveland E, Park KJ, Foo TK, Hardy CJ, 2015. Inductively coupled wireless RF coil arrays. Magn Reson Imaging 33 (3), 351–357. [PubMed: 25523607]

Chen G, Wang F, Gore JC, Roe AW, 2013. Layer-specific BOLD activation in awake monkey V1 revealed by ultra-high spatial resolution functional magnetic resonance imaging. Neuroimage 64, 147–155. [PubMed: 22960152]

Chen XM, Sobczak F, Chen Y, Jiang YY, Qian CQ, Lu ZN, Ayata C, Logothetis NK, Yu X, 2019a. Mapping optogenetically-driven single-vessel fMRI with concurrent neuronal calcium recordings in the rat hippocampus. Nat. Commun 10.

Chen Y, Pais-Roldan P, Chen X, Frosz MH, Yu X, 2019b. MRI-guided robotic arm drives optogenetic fMRI with concurrent Ca(2+) recording. Nat. Commun 10 (1), 2536. [PubMed: 31182714]

Chen Y, Sobczak F, Pais-Roldan P, Schwarz C, Koretsky AP, Yu X, 2020. Mapping the brain-wide network effects by optogenetic activation of the corpus callosum. Cerebral Cortex 30 (11), 5885–5898. [PubMed: 32556241]

Darrasse L, Ginefri JC, 2003. Perspectives with cryogenic RF probes in biomedical MRI. Biochimie 85 (9), 915–937. [PubMed: 14652180]

Desai M, Kahn I, Knoblich U, Bernstein J, Atallah H, Yang A, Kopell N, Buckner RL, Graybiel AM, Moore CI, Boyden ES, 2011. Mapping brain networks in awake mice using combined optical neural control and fMRI. J. Neurophysiol 105 (3), 1393–1405. [PubMed: 21160013]

Ferenczi EA, Zalocusky KA, Liston C, Grosenick L, Warden MR, Amatya D, Katovich K, Mehta H, Patenaude B, Ramakrishnan C, Kalanithi P, Etkin A, Knutson B, Glover GH, Deisseroth K, 2016. Prefrontal cortical regulation of brainwide circuit dynamics and reward-related behavior. Science 351 (6268).

Finn ES, Huber L, Jangraw DC, Molfese PJ, Bandettini PA, 2019. Layer-dependent activity in human prefrontal cortex during working memory. Nat Neurosci 22 (10), 1687–1695. [PubMed: 31551596]

Gao YR, Ma Y, Zhang Q, Winder AT, Liang Z, Antinori L, Drew PJ, Zhang N, 2017. Time to wake up: studying neurovascular coupling and brain-wide circuit function in the un-anesthetized animal. Neuroimage 153, 382–398. [PubMed: 27908788]

Gareis D, Wichmann T, Lanz T, MeIkus G, Horn M, Jakob PM, 2007. Mouse MRI using phased-array coils. NMR Biomed. 20 (3), 326–334. [PubMed: 17451179]

Ginefri JC, Rubin A, Tatoulian M, Woytasik M, Boumezbeur F, Djemai B, Poirier-Quinot M, Lethimonnier F, Darrasse L, Dufour-Gergam E, 2012. Implanted, inductively-coupled, radiofrequency coils fabricated on flexible polymeric material: application to *in vivo* rat brain MRI at 7 T. J. Magnet. Resonance 224, 61–70.

Goense JBM, Logothetis NK, 2006. Laminar specificity in monkey V1 using high-resolution SE-fMRI. Magn. Reson. Imaging 24 (4), 381–392. [PubMed: 16677944]

Han S, Eun S, Cho H, Uludag K, Kim SG, 2021. Improvement of sensitivity and specificity for laminar BOLD fMRI with double spin-echo EPI in humans at 7 T. Neuroimage 241, 118435. [PubMed: 34324976]

He Y, Wang M, Chen X, Pohmann R, Polimeni JR, Scheffler K, Rosen BR, Kleinfeld D, Yu X, 2018. Ultra-slow single-vessel BOLD and CBV-based fMRI spatiotemporal dynamics and their correlation with neuronal intracellular calcium signals. Neuron 97 (4), 925–939 e925. [PubMed: 29398359]

Hoffmeyer HW, Enager P, Thomsen KJ, Lauritzen MJ, 2007. Nonlinear neurovascular coupling in rat sensory cortex by activation of transcallosal fibers. J. Cerebral Blood Flow Metabol 27 (3), 575–587.

Huber L, Handwerker DA, Jangraw DC, Chen G, Hall A, Stuber C, Gonzalez–Castillo J, Ivanov D, Marrett S, Guidi M, Goense J, Poser BA, Bandettini PA, 2017. High-resolution CBV-fMRI allows mapping of laminar activity and connectivity of cortical input and output in human M1. Neuron 96 (6), 1253 -+. [PubMed: 29224727]

Iordanova B, Vazquez A, Kozai TDY, Fukuda M, Kim SG, 2018. Optogenetic investigation of the variable neurovascular coupling along the interhemispheric circuits. J. Cerebral Blood Flow Metabol. 38 (4), 627–640.

Jung WB, Im GH, Jiang H, Kim SG, 2021. Early fMRI responses to somatosensory and optogenetic stimulation reflect neural information flow. Proc. Natl. Acad. Sci. USA 118 (11).

Karayannis T, Huerta-Ocampo I, Capogna M, 2007. GABAergic and pyramidal neurons of deep cortical layers directly receive and differently integrate callosal input. Cerebral Cortex 17 (5), 1213–1226. [PubMed: 16829551]

Kashyap S, Ivanov D, Havlicek M, Sengupta S, Poser BA, Uludag K, 2018. Resolving laminar activation in human V1 using ultra-high spatial resolution fMRI at 7T. Sci. Rep 8.

Kawaguchi Y, 1992. Receptor subtypes involved in callosally-induced postsynaptic potentials in rat frontal agranular cortex invitro. Exp Brain Res 88 (1), 33–40. [PubMed: 1347272]

Kumar SS, Huguenard JR, 2001. Properties of excitatory synaptic connections mediated by the corpus callosum in the developing rat neocortex. J. Neurophysiol 86 (6), 2973–2985. [PubMed: 11731554]

Lake EMR, Ge X, Shen X, Herman P, Hyder F, Cardin JA, Higley MJ, Scheinost D, Papademetris X, Crair MC, Constable RT, 2020. Simultaneous cortex-wide fluorescence Ca(2+) imaging and whole-brain fMRI. Nat. Methods 17 (12), 1262–1271. [PubMed: 33139894]

Lee AT, Gee SM, Vogt D, Patel T, Rubenstein JL, Sohal VS, 2014. Pyramidal neurons in prefrontal cortex receive subtype-specific forms of excitation and inhibition. Neuron 81 (1), 61–68. [PubMed: 24361076]

Lee JH, Durand R, Gradinaru V, Zhang F, Goshen I, Kim DS, Fenno LE, Ramakrishnan C, Deisseroth K, 2010. Global and local fMRI signals driven by neurons defined optogenetically by type and wiring. Nature 465 (7299), 788–792. [PubMed: 20473285]

Liang Z, Ma Y, Watson GDR, Zhang N, 2017. Simultaneous GCaMP6-based fiber photometry and fMRI in rats. J. Neurosci. Methods 289, 31–38. [PubMed: 28687521]

Liang Z, Watson GD, Alloway KD, Lee G, Neuberger T, Zhang N, 2015. Mapping the functional network of medial prefrontal cortex by combining optogenetics and fMRI in awake rats. Neuroimage 117, 114–123. [PubMed: 26002727]

Logothetis NK, 2008. What we can do and what we cannot do with fMRI. Nature 453 (7197), 869–878. [PubMed: 18548064]

Logothetis NK, 2010. Bold claims for optogenetics. Nature 468 (7323), E3–E4. [PubMed: 21107378]

Logothetis NK, Pauls J, Augath M, Trinath T, Oeltermann A, 2001. Neurophysiological investigation of the basis of the fMRI signal. Nature 412 (6843), 150–157. [PubMed: 11449264]

Mett RR, Sidabras JW, Hyde JS, 2016. MRI surface-coil pair with strong inductive coupling. Rev. Sci. Instruments 87 (12).

Moon HS, Jiang H, Vo TT, Jung WB, Vazquez AL, Kim SG, 2021. Contribution of Excitatory and Inhibitory Neuronal Activity to BOLD fMRI. Cereb Cortex 31 (9), 4053–4067. [PubMed: 33895810]

Nunes D, Ianus A, Shemesh N, 2019. Layer-specific connectivity revealed by diffusion-weighted functional MRI in the rat thalamocortical pathway. Neuroimage 184, 646–657. [PubMed: 30267858]

Ogawa S, Tank DW, Menon R, Ellermann JM, Kim SG, Merkle H, Ugurbil K, 1992. Intrinsic Signal Changes Accompanying Sensory Stimulation - Functional Brain Mapping with Magnetic-Resonance-Imaging. Proc. Natl. Acad. Sci. USA 89 (13), 5951–5955. [PubMed: 1631079]

Pais-Roldan P, Takahashi K, Sobczak F, Chen Y, Zhao X, Zeng H, Jiang Y, Yu X, 2020. Indexing brain state-dependent pupil dynamics with simultaneous fMRI and optical fiber calcium recording. Proc. Natl. Acad. Sci. USA 117 (12), 6875–6882. [PubMed: 32139609]

Palmer LM, Schulz JM, Murphy SC, Ledergerber D, Murayama M, Larkum ME, 2012. The Cellular Basis of GABA(B)-Mediated Interhemispheric Inhibition. Science 335 (6071), 989–993. [PubMed: 22363012]

Peter Styles NFS, Christopher A Scott, 1989. An improved cryogenically cooled probe for high-resolution NMR. J. Magnet. Reson 84 (2), 376–378.

Poplawsky AJ, Fukuda M, Kim SG, 2019. Foundations of layer-specific fMRI and investigations of neurophysiological activity in the laminarized neocortex and olfactory bulb of animal models. Neuroimage 199, 718–729. [PubMed: 28502845]

Poplawsky AJ, Fukuda M, Murphy M, Kim SG, 2015. Layer-specific fMRI responses to excitatory and inhibitory neuronal activities in the olfactory bulb. J Neurosci 35 (46), 15263–15275. [PubMed: 26586815]

Qian CQ, Yu X, Chen DY, Dodd S, Bouraoud N, Pothayee N, Chen Y, Beeman S, Bennett K, Murphy-Boesch J, Koretsky A, 2013. Wireless amplified nuclear MR detector (WAND) for high-spatial-resolution mr imaging of internal organs: preclinical demonstration in a rodent model. Radiology 268 (1), 228–236. [PubMed: 23392428]

Qian W, Yu X, Qian CQ, 2020. Wireless reconfigurable RF detector array for focal and multiregional signal enhancement. Ieee Access 8, 136594–136604. [PubMed: 33747678]

Raimondo L, Knapen T, Oliveira IAF, Yu X, Dumoulin SO, van der Zwaag W, Siero JCW, 2021. A line through the brain: implementation of human line-scanning at 7T for ultra-high spatiotemporal resolution fMRI. J. Cerebral Blood Flow Metabol 41 (11), 2831–2843.

Rock C, Apicella AJ, 2015. Callosal projections drive neuronal-specific responses in the mouse auditory cortex. J. Neurosci 35 (17), 6703–6713. [PubMed: 25926449]

Roemer PB, Edelstein WA, Hayes CE, Souza SP, Mueller OM, 1990. The Nmr phased-array. Magn. Reson. Med 16 (2), 192–225. [PubMed: 2266841]

Ryali S, Shih YYI, Chen TW, Kochalka J, Albaugh D, Fang ZN, Supekar K, Lee JH, Menon V, 2016. Combining optogenetic stimulation and fMRI to validate a multivariate dynamical systems model for estimating causal brain interactions. Neuroimage 132, 398–405. [PubMed: 26934644]

Sangcheon Choi YC, Zeng Hang, Biswal Bharat, Yu Xin, 2021. Laminar-specific interhemispheric connectivity mapping with bilateral line-scanning fMRI. bioRxiv.

Schlegel F, Sych Y, Schroeter A, Stobart J, Weber B, Helmchen F, Rudin M, 2018. Fiber-optic implant for simultaneous fluorescence-based calcium recordings and BOLD fMRI in mice. Nat. Protoc 13 (5), 840–855. [PubMed: 29599439]

Schnall MD, Barlow C, Subramanian VH, Leigh JS, 1986. Wireless implanted magnetic-resonance probes for invivo Nmr. J. Magnet. Reson 68 (1), 161–167.

Schulz K, Sydekum E, Krueppel R, Engelbrecht CJ, Schlegel F, Schroter A, Rudin M, Helmchen F, 2012. Simultaneous BOLD fMRI and fiber-optic calcium recording in rat neocortex. Nat. Methods 9 (6), 597–602. [PubMed: 22561989]

Sharoh D, van Mourik T, Bains LJ, Segaert K, Weber K, Hagoort P, Norris DG, 2019. Laminar specific fMRI reveals directed interactions in distributed networks during language processing. Proc. Natl. Acad. Sci. USA 116 (42), 21185–21190. [PubMed: 31570628]

Silva AC, Koretsky AP, 2002. Laminar specificity of functional MRI onset times during somatosensory stimulation in rat. Proc. Natl. Acad. Sci. USA 99 (23), 15182–15187. [PubMed: 12407177]

Takata N, Yoshida K, Komaki Y, Xu M, Sakai Y, Hikishima K, Mimura M, Okano H, Tanaka KF, 2015. Optogenetic activation of CA1 pyramidal neurons at the dorsal and ventral hippocampus evokes distinct brain-wide responses revealed by mouse fMRI. PLoS ONE 10 (3), e0121417. [PubMed: 25793741]

Vazquez AL, Fukuda M, Kim SG, 2018. Inhibitory neuron activity contributions to hemodynamic responses and metabolic load examined using an inhibitory optogenetic mouse model. Cereb Cortex 28 (11), 4105–4119. [PubMed: 30215693]

Volland NA, Mareci TH, Constantinidis I, Simpson NE, 2010. Development of an Inductively coupled MR coil system for imaging and spectroscopic analysis of an implantable bioartificial construct at 11.1 T. Magn Reson Med 63 (4), 998–1006. [PubMed: 20373400]

Wang M, He Y, Sejnowski TJ, Yu X, 2018. Brain-state dependent astrocytic Ca(2+) signals are coupled to both positive and negative BOLD-fMRI signals. Proc. Natl. Acad. Sci. USA 115 (7), E1647–E1656. [PubMed: 29382752]

Wirth ED, Mareci TH, Beck BL, Fitzsimmons JR, Reier PJ, 1993. A comparison of an inductively-coupled implanted coil with optimized surface coils for in-vivo Nmr imaging of the spinal-cord. Magn Reson Med 30 (5), 626–633. [PubMed: 8259063]

Yu X, He Y, Wang MS, Merkle H, Dodd SJ, Silva AC, Koretsky AP, 2016. Sensory and optogenetically driven single-vessel fMRI. Nat. Methods 13 (4), 337–340. [PubMed: 26855362]

Yu X, Qian CQ, Chen DY, Dodd SJ, Koretsky AP, 2014. Deciphering laminar-specific neural inputs with line-scanning fMRI. Nat. Methods 11 (1), 55 -+. [PubMed: 24240320]

Yu YH, Huber L, Yang JJ, Jangraw DC, Handwerker DA, Molfese PJ, Chen G, Ejima Y, Wu JL, Bandettini PA, 2019. Layer-specific activation of sensory input and predictive feedback in the human primary somatosensory cortex. Sci. Adv 5 (5).

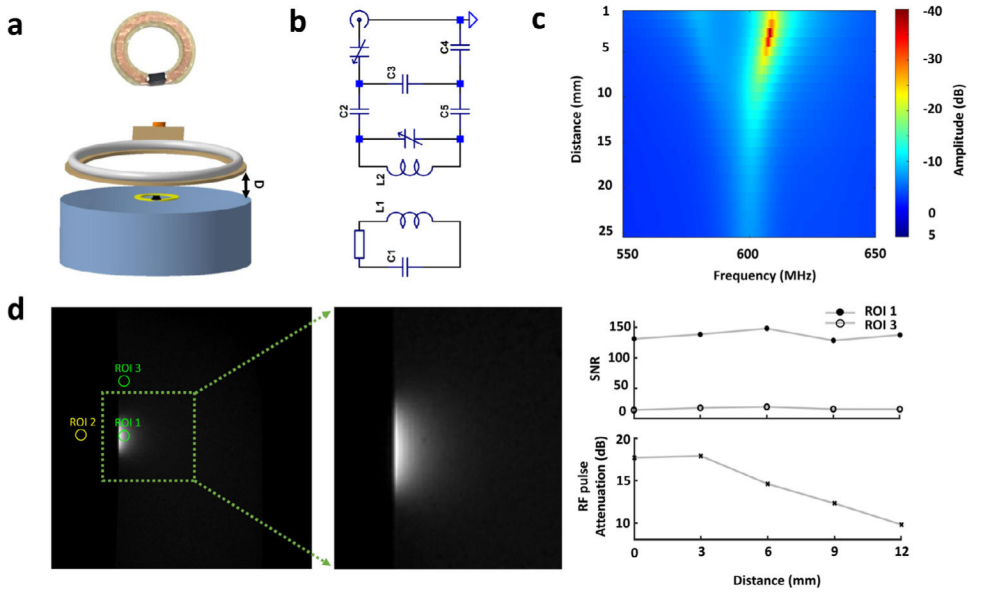

Fig. 1.

Evaluation of inductive coil under different distance separations. (a) Photograph of ICD (upper) and schematic drawing of the phantom test arrangement with the ICD placed on the surface of a 1% agarose gel. (b) Diagrams of ICD implemented as a single resonant circuit coupled inductively to the external RF surface coil. (c) Coupling performance varies with the increased distant separations between the inductive loop and the transceiver coil. (d) The intensity of the FLASH 2D image acquired from the gel phantom shows a significantly higher SNR inside the enhanced region (ROI 1) than the unenhanced region (ROI 3). The noise was measured from the ROI outside the object (ROI 2). The ICD was placed on the gel while the surface coil was separated from the gel surface by 3 mm. Left: phantom image with regions of interest for performance comparison. Right upper, spatial SNR comparison between regions with increased distance separation between the two coils. Bottom, the required attenuation of RF pulse power changes as a function of distance separation.

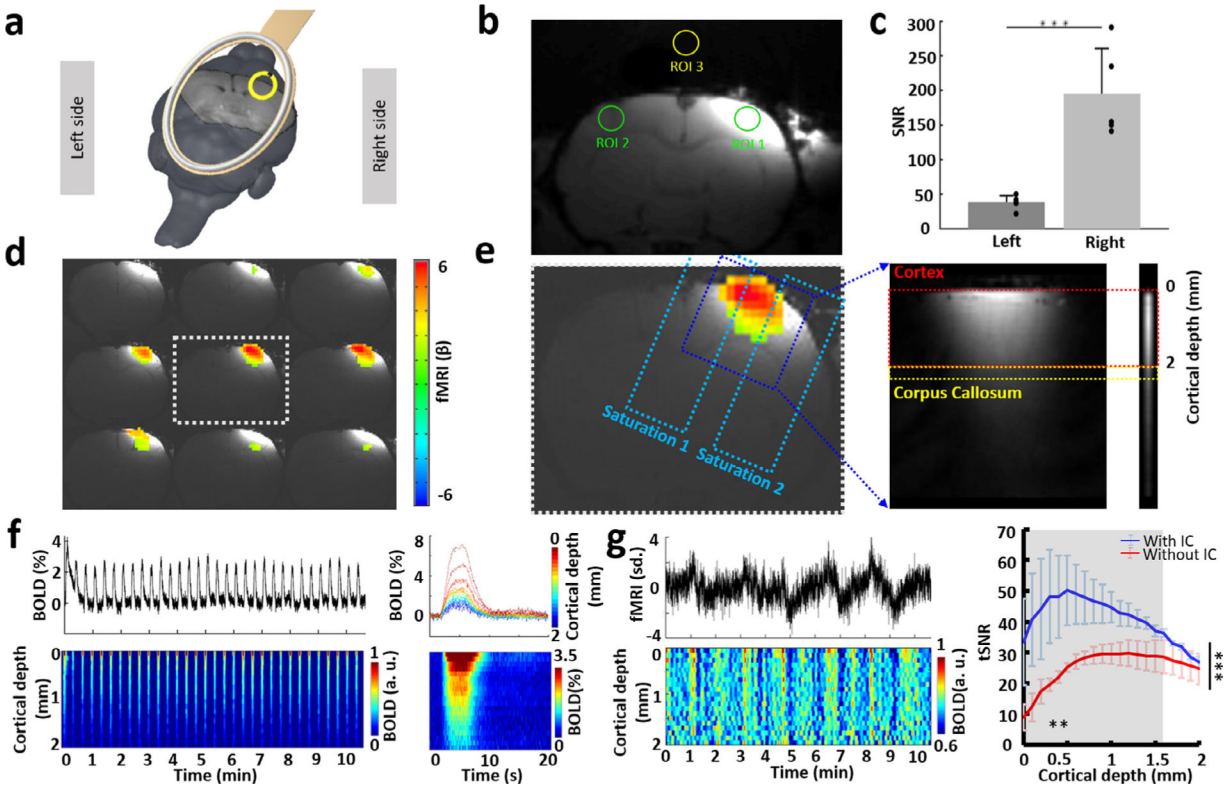

Fig. 2.

BOLD responses were detected using a unilateral line-scanning method in the enhanced region. (a) The inductive coil covers the FP-S1 region on the right hemisphere, with a surface coil covering the whole rat brain. (b) A representative anatomic image shows enhanced focal intensity in the right FP-S1 region (ROI 1). The noise was measured from the ROI outside the object (ROI 3). (c) Significantly higher SNR in ROI 1 with inductive coil (right) than in ROI 2 (left) (Paired-sample *t*-test, $***P = 7 \times 10^{-4}$, $n = 5$ rats, mean ± SD). (d) Superimposed color-coded BOLD activation map with left forepaw electrical stimulation (3 Hz, 4 s, 2 mA) on the anatomical images (FLASH). (e) The procedure to set up the unilateral line-scanning method. (f) Averaged BOLD percentage change from all 20 voxels in the cortex for 32 epochs (top left) and each epoch along with the cortical depth (top right, 20 voxels, 2 mm). Normalized spatiotemporal map (bottom left) along cortical depth for the trial (bottom left) and the epoch (bottom right) ($n = 3$ rats, 17 trials, 32 epochs, 10 min 40 s per trial). (g) Averaged time course (top left) extracted from the right cortex shows the hemodynamic fluctuation in the absence of stimulation and its voxel-specific normalized spatiotemporal map (bottom left) throughout the cortex (20 voxels, 2 mm). Right, the tSNR with the inductive coil (blue) is significantly higher than our previous results acquired with the surface coil (red). It is noteworthy that SNR close to the corpus callosum is compatible (paired-sample *t*-test, $***P < 0.001$, $**P < 0.01$ for the gray shadow, 0–1.6 mm, $n = 3$ rats, mean ± SD).

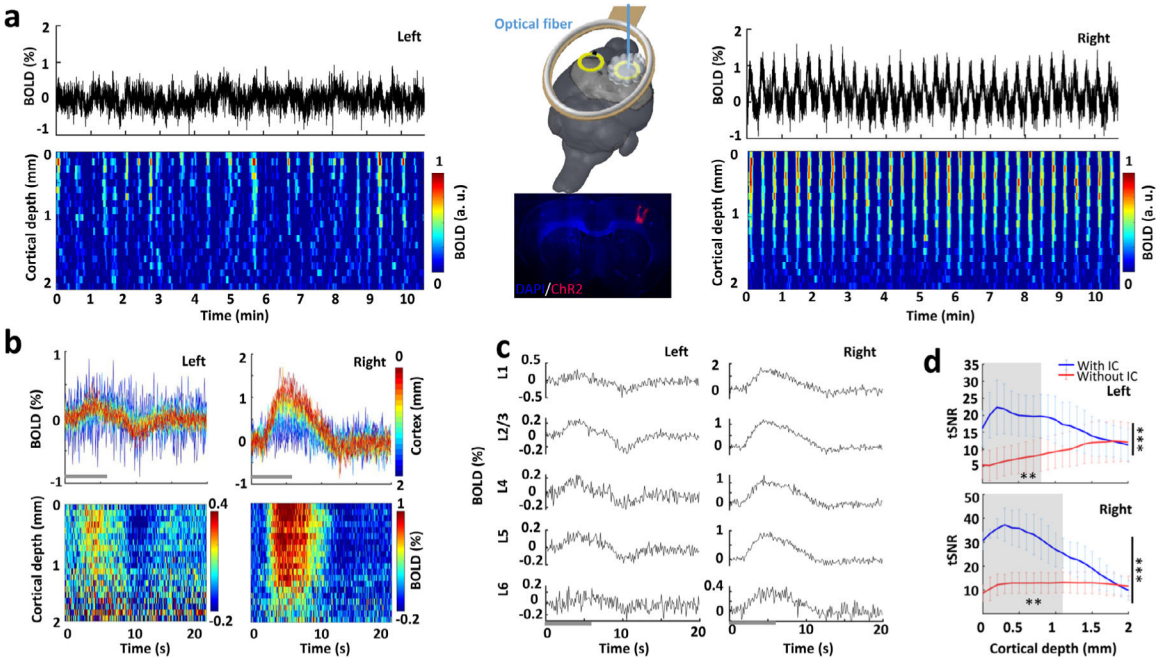

Fig. 3.

Optogenetically evoked BOLD responses in bilateral enhanced FP-S1. (a) Averaged time course (top) and normalized spatiotemporal map (bottom) of bilateral BOLD responses in FP-S1 regions induced directly by optogenetic stimulation in the right hemisphere (right) and projected left hemisphere (left, $n = 3$ rats, 49 trials, 32 epochs, 2 Hz, 6 s, 10 ms light pulse, 30 mW). The middle upper is a schematic drawing of two inductive coils stuck adjacent to bilateral hemispheres, with optical fiber (blue) inserted to the right FP-S1 region. Middle lower, a representative wide-field fluorescence image illustrates robust ChR2-mCherry expression in the right FP-S1. (b) fMRI percentage-change time courses (top) and maps (bottom) for epoch in each voxel along cortical depth on both hemispheres ($n = 3$ rats, 49 trials). gray lines indicate light stimulation. (c) Averaged epoch-wise time courses show the different laminar-specific responses of both hemispheres ($n = 3$ rats). gray lines indicate light stimulation. (d) The comparison between both hemispheres shows significantly higher tSNR in images acquired with (blue) implanted inductive coils over images acquired without (red) implanted inductive coils (paired-sample t-test, $^{***}P < 0.001$, $^{**}P < 0.01$ for the gray shadow, upper panel 0–0.8 mm, lower panel 0–1.1 mm, $n = 3$ rats, mean ± SD). The asterisks on the right side indicate a 3-fold sensitivity gain.